Monthly Notices
of the
ROYAL ASTRONOMICAL SOCIETY

Mon. Not. R. Astron. Soc. **412,** 1151–1161 (2011) doi:10.1111/j.1365-2966.2010.17971.x

Herschel-ATLAS: statistical properties of Galactic cirrus in the GAMA-9 Hour Science Demonstration Phase Field

A. Bracco,[1] A. Cooray,[1,2⋆] M. Veneziani,[1,3] A. Amblard,[1] P. Serra,[1] J. Wardlow,[1] M. A. Thompson,[4] G. White,[5,6] R. Auld,[7] M. Baes,[8] F. Bertoldi,[9] S. Buttiglione,[10] A. Cava,[11] D. L. Clements,[12] A. Dariush,[7] G. De Zotti,[10,13] L. Dunne,[14] S. Dye,[7] S. Eales,[7] J. Fritz,[8] H. Gomez,[7] R. Hopwood,[5] I. Ibar,[15] R. J. Ivison,[15,16] M. Jarvis,[4] G. Lagache,[17,18] M. G. Lee,[19] L. Leeuw,[20] S. Maddox,[14] M. Michałowski,[16] C. Pearson,[5,21,22] M. Pohlen,[7] E. Rigby,[14] G. Rodighiero,[23] D. J. B. Smith,[14] P. Temi,[24] M. Vaccari[23] and P. van der Werf[16,25]

[1]*Department of Physics & Astronomy, University of California, Irvine, CA 92697, USA*
[2]*Division of Physics, Math & Astronomy, California Institute of Technology, Pasadena, CA 91125, USA*
[3]*Spitzer Science Center, California Institute of Technology, Pasadena, CA 91125, USA*
[4]*Centre for Astrophysics Research, Science and Technology Research Institute, University of Hertfordshire, Herts AL10 9AB*
[5]*Department of Physics & Astronomy, The Open University, Walton Hall, Milton Keynes MK7 6AA*
[6]*Space Science & Technology Division, The Rutherford Appleton Laboratory, Chilton, Oxfordshire OX11 0NL*
[7]*School of Physics and Astronomy, Cardiff University, The Parade, Cardiff, CF24 3AA*
[8]*Sterrenkundig Observatorium, Universiteit Gent, Krijgslaan 281 S9,B-9000 Gent, Belgium*
[9]*INAF - Osservatorio Astronomico di Padova, Vicolo Osservatorio 5, I-35122 Padova, Italy*
[10]*Argelander-Institute for Astronomy, University of Bonn, Auf dem Huegel 71, D-53121 Bonn, Germany*
[11]*Instituto de Astrofsica de Canarias and Departamento de Astrofisica - Universidad de La Laguna, E38205 La Laguna, Spain*
[12]*Astrophysics Group, Physics Department, Imperial College, Prince Consort Road, London SW7 2AZ*
[13]*SISSA, Via Bonomea 265, I-34136 Trieste, Italy*
[14]*School of Physics and Astronomy, University of Nottingham, University Park, Nottingham NG7 2RD*
[15]*UK Astronomy Technology Centre, Royal Observatory, Edinburgh EH9 3HJ*
[16]*SUPA, Institute for Astronomy, University of Edinburgh, Royal Observatory, Blackford Hill, Edinburgh EH9 3HJ*
[17]*Univ Paris-Sud, Laboratoire IAS, UMR8617, Orsay F-91405, France*
[18]*CNRS, Orsay F-91405, France*
[19]*Department of Physics and Astronomy, Seoul National University, Seoul 151-742, Korea*
[20]*SETI Institute, 515 N. Whisman Avenue, Mountain View, CA 94043, USA*
[21]*Space Science & Technology Department, The Rutherford Appleton Laboratory, Chilton, Oxfordshire OX11 0QX*
[22]*Institute for Space Imaging Science, University of Lethbridge, Lethbridge, Alberta T1K 3M4, Canada*
[23]*Department of Astronomy, University of Padova, Vicolo Osservatorio 3, Padova, Italy*
[24]*Astrophysics Branch, NASA Ames Research Center, Mail Stop 245-6, Moffett Field, CA 94035, USA*
[25]*Leiden Observatory, Leiden University, PO Box 9513, NL - 2300 RA Leiden, the Netherlands*

Accepted 2010 November 2. Received 2010 November 2; in original form 2010 September 25

ABSTRACT

We study the spectral energy distribution (SED) and the power spectrum of Galactic cirrus emission observed in the 14 deg^2 Science Demonstration Phase field of the *Herschel*-ATLAS using *Herschel* and *IRAS* data from 100 to 500 μm. We compare the Spectral and Photometric Imaging Receiver (SPIRE) 250, 350 and 500 μm maps with *IRAS* 100-μm emission, binned in 6-arcmin pixels. We assume a modified blackbody SED with dust emissivity parameter β ($F \propto \lambda^{-\beta}$) and a single dust temperature $T_{\rm d}$, and find that the dust temperature and emissivity index varies over the science demonstration field as $10 < T_{\rm d} < 25\,{\rm K}$ and $1 < \beta < 4$. The latter values are somewhat higher than the range of β often quoted in the literature

⋆E-mail: acooray@uci.edu

($1 < \beta < 2$). We estimate the mean values of these parameters to be $T_{\rm d} = 19.0 \pm 2.4$ K and $\beta = 1.4 \pm 0.4$. In regions of bright cirrus emission, we find that the dust has similar temperatures with $T_{\rm d} = 18.0 \pm 2.5$ K, and similar values of β, ranging from 1.4 ± 0.5 to 1.9 ± 0.5. We show that $T_{\rm d}$ and β associated with diffuse cirrus emission are anti-correlated and can be described by the relationship: $\beta(T_{\rm d}) = NT_{\rm d}^{\alpha}$ with $[N = 116 \pm 38, \alpha = -1.4 \pm 0.1]$. The strong correlation found in this analysis is not just limited to high-density clumps of cirrus emission as seen in previous studies, but is also seen in diffuse cirrus in low-density regions. To provide an independent measure of $T_{\rm d}$ and β, we obtain the angular power spectrum of the cirrus emission in the *IRAS* and SPIRE maps, which is consistent with a power spectrum of the form $P(k) = P_0(k/k_0)^{\gamma}$, where $\gamma = 2.6 \pm 0.2$ for scales of 50–200 arcmin in the SPIRE maps. The cirrus rms fluctuation amplitude at angular scales of 100 arcmin is consistent with a modified blackbody SED with $T_{\rm d} = 20.1 \pm 0.9$ K and $\beta = 1.3 \pm 0.2$, in agreement with the values obtained above.

Key words: methods: statistical – ISM: structure – infrared: ISM.

1 INTRODUCTION

The submillimetre (submm) and millimetre emission of diffuse Galactic dust is primarily determined by the thermal radiation of large dust grains that are in equilibrium with the interstellar radiation field (Désert, Boulanger & Puget 1990). The dust organizes itself into large-scale structures such as cirrus and filaments both at low and high Galactic latitudes (Low et al. 1984). To compare with previous studies, we approximate the dust emission by a single thermal Planck spectrum at the temperature $T_{\rm d}$ of the grains modified by a power-law dependence on frequency parametrized by the spectral emissivity parameter β in the optically thin approximation:

$$I(\nu) = \epsilon(\nu) B(\nu, T_{\rm d}) N_{\rm H}\,, \tag{1}$$

where $I(\nu)$ is the specific brightness, B_ν is the Planck spectrum, and $N_{\rm H}$ is the total hydrogen column density along the line of sight. The isothermal assumption is likely to be only approximate. While at high latitudes the overlap of several dust sources along the line of sight is expected to be small, we still expect a complex temperature structure due to variations in the grain size distribution and any variations in the radiation field. In the above equation, $\epsilon(\nu)$ is the emissivity:

$$\epsilon(\nu) = X_{\rm d}\epsilon_0 \left(\frac{\nu}{\nu_0}\right)^{\beta} \tag{2}$$

where $X_{\rm d}$ is the dust-to-gas mass ratio and ϵ_0 is the emissivity at frequency ν_0.

With $T_{\rm d}$ at the level of 10–30 K the maximum intensity is found at far-infrared (far-IR)/submm wavelengths. Due to the lack of coverage at far-IR wavelengths, studies on the Galactic cirrus temperature and emissivity before *Herschel*[1] (Pilbratt et al. 2010) focused on the wavelength bands shorter than 160 μm that were covered by *IRAS* and *Spitzer* (e.g. Miville-Deschênes, Lagache & Puget 2002; Jeong et al. 2005), longer than 1 mm covered by various cosmic microwave background (CMB) experiments (e.g. Désert et al. 2009; Veneziani et al. 2010), and a combination including limited submm data (e.g. Bernard et al. 1999; Dupac et al. 2003; Paradis, Bernard & Mény 2009).

[1] *Herschel* is an European Space Agency (ESA) space observatory with science instruments provided by European-led Principal Investigator consortia and with important participation from NASA.

With its unprecedented angular resolution and the ability to cover wide fields by scanning across the sky, the Spectral and Photometric Imaging Receiver (SPIRE; Griffin et al. 2010) on *Herschel* now allows for the first time the possibility to study the structure of the interstellar medium (ISM) at tens of arcseconds to degree angular scales at the peak of the dust spectral energy distribution (SED). At the smallest angular scales probed by SPIRE, the structure of the diffuse ISM provides information about the initial conditions for the formation of dense molecular clouds. Some of these clouds may be on the verge of gravitational collapse leading to the formation of a new star (Olmi et al. 2010; Sadavoy, Di Francesco & Johnstone 2010; Ward-Thompson et al. 2010). At large angular scales, dust is a key tracer of the large-scale physical processes occurring in the diffuse ISM (Miville-Deschênes et al. 2010). Dust emission is also related to the density structure of diffuse clouds and could potentially provide a way to study the projected density distribution within the Galactic cirrus.

In equation (2), the dust emissivity index β provides information on the physical nature of dust and connects the grain structure to the large-scale environmental density. The spectral index of the emissivity depends on grain composition, temperature distribution of tunnelling states and the wavelength-dependent excitation (e.g. Meny et al. 2007). The emissivity β is also expected to vary with wavelength when the dust temperature is intrinsically multicomponent but described by an isothermal model (Paradis et al. 2009). While the dust SED models in the literature generally assume a fixed value for the spectral emissivity β between 1.5 and 2.5, there might be significant variations in β, even in a small cirrus region, when taking into account the disordered structure of dust grains. There are also however the uncertainties associated with the dust size distribution and the silicate versus graphite fractions; large variations in both these quantities could result in different equilibrium temperatures even in a small cirrus region. This complicates any physical interpretation of β and $T_{\rm d}$ when using an isothermal SED. Instead of multicomponent models, we use the isothermal model here so that we can compare our results to previous analyses that make the same assumption. Our SED modelling is also limited to four data points. Of particular interest to this work is the suggestion that β and $T_{\rm d}$ are inversely related in high-density environments of Galactic dust by previous observations in the submm and millimetre domain, both at low (Dupac et al. 2003; Désert et al. 2009) and high (Veneziani et al. 2010) Galactic latitudes.

Most of the recent studies on properties of the Galactic cirrus focused on high-density environments, such as cold clumps and molecular clouds with intensities of order 100 MJy sr^{-1} or more at far-IR wavelengths (see, however, Bot et al. 2009 for a study on diffuse medium at small scales). Properties of the ISM at high latitudes, especially involving diffuse cirrus with intensities of order a few MJy sr^{-1}, are still not well known. A good modelling of diffuse dust distribution and its characteristics in the high-latitude regions is necessary in order to remove its contamination from CMB anisotropy measurements (see e.g. Leach et al. 2008 and Ricciardi et al. 2010). The CMB community primarily relies on models developed with *IRAS* and Diffuse Infrared Background Experiment (DIRBE) maps to describe the dust distribution (e.g. Schlegel, Finkbeiner & Davis 1998) and the frequency dependence of the intensity (e.g. Finkbeiner, Davis & Schlegel 1999). With wide-field *Herschel*-ATLAS (H-ATLAS; Eales et al. 2010) maps we can study the dust temperature and emissivity variation across large areas on the sky, first in the Science Demonstration Phase (SDP) field covering 14 deg^2 and eventually over 550 deg^2 spread over five fields with varying Galactic latitudes. The H-ATLAS SDP patch is at a Galactic latitude of $\sim$30°. Combining SPIRE data at 250, 350 and 500 μm with *IRAS* maps of the same area at 100 μm allows us to sample the peak of the dust SED accurately.

Here we present an analysis of diffuse Galactic cirrus in the H-ATLAS SDP field from 100 to 500 μm using *IRAS* and *Herschel*-SPIRE maps. We derive physical parameters of the diffuse dust at arcminute angular scales such as the temperature and spectral emissivity parameter and their relationship to each other. We also present a power spectrum analysis of the cirrus emission, which allows us to study the spatial structure of the ISM from tens of arcseconds to degree angular scales. The discussion is organized as follows. Section 2 describes the data sets and Section 3 describes the pipeline adopted. Section 4 reports results related to the temperature and spectral emissivity parameter, while Section 5 describes the cirrus power spectrum. We conclude with a summary in Section 6.

2 DATA SETS

We use *Herschel*-SPIRE maps in the H-ATLAS 14 deg.^{2} SDP field, centred at RA = $9^{\rm h}25^{\rm m}31^{\rm s}$, Dec. = $0°29'58''$, overlapping with the Galaxy and Mass Assembly (GAMA) survey (Driver et al. 2009). In addition to the three SPIRE bands, we also use the *IRAS* 100-μm map. The latter is obtained by IDL routines projecting the HEALPIX[2] format map made by the IRIS processing system of the *IRAS* survey[3] (Miville-Deschênes & Lagache 2005).

We refer the reader to Pascale et al. (2011) for details on the H-ATLAS SPIRE map-making procedure and basic details related to the maps. Since we are interested in the diffuse emission, we make use of a set of maps that have been especially made to preserve the extended structure by accounting for the map-making transfer function. We also produced a second set of maps using the same timelines processed by the *Herschel* Interactive Processing Environment (HIPE; Ott et al. 2006), but with an independent map-making pipeline. This involved the use of an iterative approach to make new maps using SHIM v1.0 (the SPIRE-HerMES Iterative Mapper; Levenson et al. 2010). For that map maker simulations show a transfer function that is close to unity over arcminute to degree angular scales. The results we describe here, however, are consistent within overall uncertainties between the two sets of maps. Thus, we describe results primarily using the H-ATLAS map-making pipeline of Pascale et al. (2011). We do not use the H-ATLAS Photodetector Array Camera and Spectrometer (PACS) SDP maps for this analysis, since the diffuse emission at short wavelengths imaged by PACS is heavily filtered out during the map-making process as carried out in the production of H-ATLAS PACS SDP data products (Ibar et al. 2010).

[2] http://healpix.jpl.nasa.gov
[3] http://www.cita.utoronto.ca/ mamd/IRIS/

3 DATA ANALYSIS

The aim of this paper is to characterize the physical properties of dust emission over the whole SDP area. In order to avoid contamination of our Galactic dust measurements from extragalactic point sources, we first remove the bright detected sources from each of the maps making use of the H-ATLAS source catalogues (Rigby et al. 2011). This catalogue involves sources that have been detected at 5σ in at least one of the bands. Given that SPIRE data have beam sizes of approximately 18, 25 and 36 arcsec, respectively, at 250, 350 and 500 μm, we introduce a source mask by simply setting the pixel values over a square size of 20, 30 and 40 arcsec to be zero at the source locations. For a handful of extended sources in the Rigby et al. (2011) catalogue, we increased the size of the mask based on the source size as estimated directly from maps. With close to 6700 sources in total, this masking procedure involved a removal of 2, 5 and 6 per cent of the data at 250, 350 and 500 μm, respectively. Removal of such a small fraction of pixels does not bias our results. Alternatively, we could have modelled each source by fitting the point spread function at each of the source locations and removing the flux associated with the source and retaining the background; we ran a set of simulations to study if the two approaches lead to different results, but we did not find any. In the case of the 100-μm *IRAS* map, we similarly masked roughly 35 point sources in the SDP area from the *IRAS*-Faint Source Catalogue of Wang & Rowan-Robinson (2009) by setting the pixel intensity to be zero over a square area of size 6 arcsec. We also found consistent results when we replace all *IRAS* pixels above 5σ with zero intensity.

To compare the *IRAS* and *Herschel* maps, we then convolve the source-masked SPIRE maps to the angular resolution of the *IRAS* 100-μm map (258 arcsec full width at half-maximum) and repixelize SPIRE maps at the same pixel scale as *IRAS* (120-arcsec pixel sizes). For the *IRAS* map, the flux errors are estimated by assuming that noise is isotropic and using the IRIS noise estimate (Miville-Deschênes & Lagache 2005). For SPIRE, we use the noise maps produced by taking the differences of repeated scans (Pascale et al. 2011) and convolve the noise map to the *IRAS* 100-μm angular resolution and *IRAS* pixel size.

4 DUST SPECTRAL ENERGY DISTRIBUTION

To describe the SED we use a modified blackbody spectrum with a spectral emissivity β in the optically thin limit such that

$$S(\nu) = A \left(\frac{\nu}{\nu_0}\right)^{\beta} B_\nu(T_{\rm d}), \tag{3}$$

where the amplitude A depends on the optical depth through the dust, β is the spectral emissivity, and $T_{\rm d}$ is the temperature of the dust. We take $\nu_0 = 3$ THz corresponding to the *IRAS* 100-μm measurement.

To estimate the best-fitting values for the three unknown parameters (A, β, $T_{\rm d}$), we make use of a Markov Chain Monte Carlo

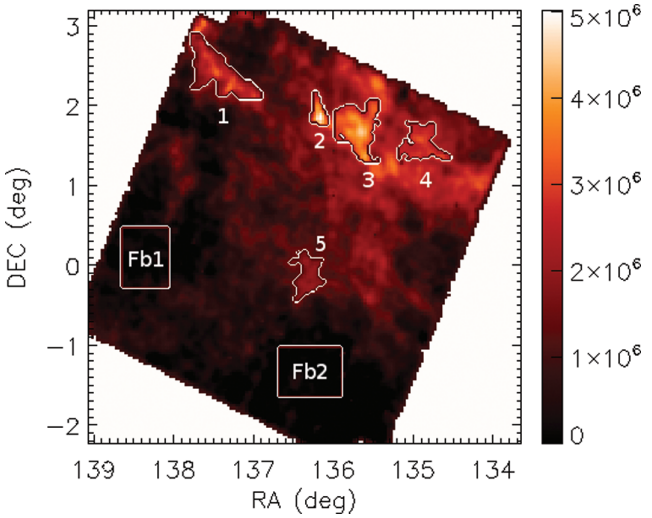

Figure 1. Selected regions of high-cirrus intensity that we have individually analysed (labelled 1–5) as well as the two low-cirrus regions (labelled Fb1 and Fb2) that we used to account for the extragalactic background intensity. The map, at 250 μm, is colour coded in intensity units of Jy sr^{-1}.

(MCMC) approach (Lewis & Bridle 2002). We are able to generate the MCMC chains rapidly and at the same time fully sample the likelihood functions of the model parameters. Appropriate sampling of the likelihood is crucial to study the relation between β and $T_{\rm d}$ (Section 4.4).

The model fits adopt uniform priors over a wide range with β between -1 and 6, and $T_{\rm d}$ between 1 and 50 K so that we do not incorrectly constrain the best-fitting values by a narrow range of priors. The ranges are set such that we also allow both the minimum and maximum values of β and $T_{\rm d}$ to be well outside the expected extremes. We run MCMC chains for each region until we get convergence based on the Gelman and Rubin statistic (Gelman & Rubin 1992), with a value for $1 - R$ of at least 0.01, where R is defined as the ratio between the variance of chain means and the mean of the variances.

4.1 Zero-level in SPIRE maps

Since the SPIRE maps are not absolutely calibrated, to study the dust temperature over the SDP region as a whole (Fig. 1), we account for the zero-point offset through the pixel-correlation method of Miville-Deschênes et al. (2010). Before computing the correlation, we remove a constant intensity corresponding to the extragalactic background at 100 μm from the *IRAS* map (0.78 MJy sr^{-1}; Lagache et al. 2000; Miville-Deschênes et al. 2002). We then correlate the *IRAS* pixel intensity with that of a SPIRE map at the corresponding pixel. Here we use the source-masked SPIRE maps repixelized to the *IRAS* pixel scale following the procedure described in Section 3.

We show this correlation in Fig. 2, where we plot the pixel intensity values at the three SPIRE bands as a function of the *IRAS* intensity. We minimize the difference between $\sum_{ij}[S_{ij}(\lambda) - P_{ij}(\lambda)]$, where $S_{ij}(\lambda)$ is the SPIRE intensity at pixel (i, j) at waveband λ and $P_{ij}(\lambda)$ is the predicted SPIRE flux in each of the pixels by scaling *IRAS* 100-μm map intensity $I(100)$, with the assumption that $P_{ij}(\lambda) = G \times I_{ij}(100) + S_0$, where G, submm colour (also called 'gain' in Miville-Deschênes et al. 2010), and S_0, the zero-point offset, are the mean values over the whole of the map. This is correct for the additive (S_0) term under the assumption that the *IRAS* map is a

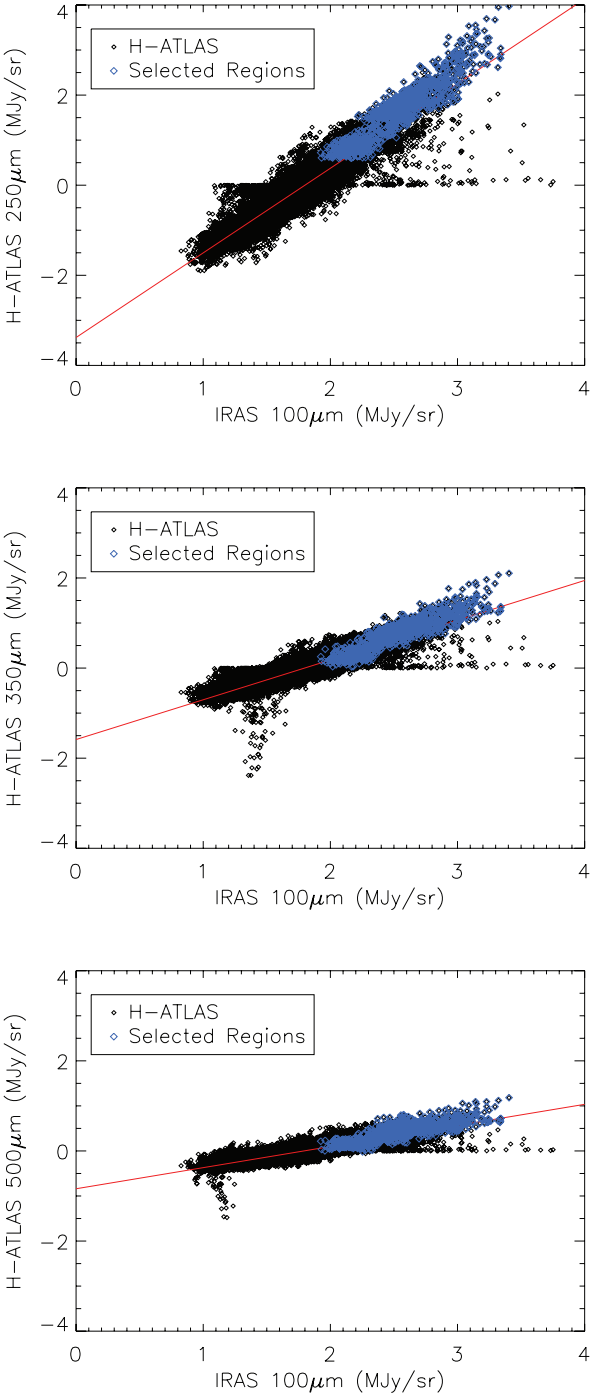

Figure 2. The *IRAS* 100-μm intensity versus SPIRE intensity at 250 (top), 350 (middle) and 500 (bottom) μm. The SPIRE maps are pixelized to *IRAS*, and we use the relation between SPIRE intensity and *IRAS* intensity to determine the submm colour and zero-point offset relative to the *IRAS* map (see text for details). The points coloured blue are from the bright cirrus regions marked 1–5 in Fig. 1. The points with zero values to SPIRE intensity are pixels that remain zero after smoothing to *IRAS* pixel scale due to our point and extended source masks that were defined in the original pixel scale. These and other points that fall off the main band of points, possibly associated with issues related to parts of the time-streams that are either contaminated or contain glitches that were removed, do not bias the colour and zero-point offset estimates.

true reflection of the sky. The estimated values of G are 1.9 ± 0.3, 0.9 ± 0.3 and 0.5 ± 0.1 at 250, 350 and 500 μm respectively, while S_0 takes the values of $-(3.2 \pm 1.0)$, $-(1.5 \pm 0.6)$, $-(0.8 \pm 0.4)$ MJy sr^{-1} at each of the three frequencies.

The uncertainty in submm colour G is estimated by taking the rms of the ratio involving $S(\lambda)/I(100)$ once the offset S_0 is removed from each of the maps, while the uncertainty in S_0 comes from the rms of the difference involving $S(\lambda) - G \times I(100)$, with the best-fitting values for submm colour used in the computation. As described in Miville-Deschênes et al. (2010), these rms values reflect the overall uncertainties more accurately than if one were to simply use the statistics associated with the linear fit to the relation between $S(\lambda)$ and $I(100)$. Those have uncertainties that are at least a factor of 10 smaller than the errors quoted above. Fig. 2 shows points which show zero fluxes in SPIRE maps or are significantly negative; these are associated with a combination of the source mask and pixels that were associated with parts of the time-streams that are either contaminated or contain glitches that were removed. The correlation analysis above accounts for such pixels when degrading the resolution, and we find that such points do not bias the colour and zero-point offset estimates we have quoted above.

The mean intensity of the SPIRE maps in the SDP field, once corrected for S_0, is around $(4.8, 2.5, 1.6)$ (± 0.5) MJy sr^{-1} at 250, 350 and 500 μm, respectively. These can be compared to the estimated extragalactic background intensity at each of the three frequencies of 0.85, 0.69 and 0.39 MJy sr^{-1} with an uncertainty at the level of 0.1 MJy sr^{-1} (Fixsen et al. 1998). The SDP field, on average, is a factor of 4–5 brighter than the extragalactic background. The lowest pixel intensity values of the SDP field in Fig. 2 (once corrected for S_0) allow an independent constraint on the extragalactic background intensity, but such a study is best attempted in fields where the overall cirrus intensity is similar to or smaller than the expected extragalactic background. Fields that span over a wide range of Galactic longitudes and latitudes are also desirable since such fields allow an additional constraint on determining a constant intensity that is independent of the location. We will attempt such studies in future works making use of multiple fields in H-ATLAS.

Beyond the mean intensity, the extragalactic background arising from sources below the confusion noise has been shown to fluctuate at the few per cent level at 30-arcmin angular scales (Amblard et al. 2011). Those faint sources are also responsible for roughly 85 per cent of the extragalactic background intensity (Clements et al. 2010; Oliver et al. 2010). We are not able to account for the contamination coming from the unresolved extragalactic background light, but the fluctuation intensity of 0.1 MJy sr^{-1} at 30-arcmin angular scales do not bias the measurements we report here. The background fluctuations act as an extra source of uncertainty in our measurements as they introduce an extra scatter in the intensity measurements from one region to another and that scatter is captured in the overall error budget.

4.2 Average dust SED

Combining the *IRAS* 100-μm average cirrus intensity over the whole SDP area (1.77 MJy sr^{-1}) with the above submm colour factors, and assuming a 15 per cent flux uncertainty coming from the overall calibration of SPIRE (Swinyard et al. 2010), we estimate the dust temperature T_d and β to be 19.0 ± 2.4 K and 1.4 ± 0.4, respectively (Fig. 3). The same SED can also be described by the two temperature model of Finkbeiner et al. (1999), where we fix $T_d = 9.2$ and 16.2 K and $\beta = 1.67$ and 2.7, with the SED computed using the maps derived from Schlegel et al. (1998) dust map following an analysis similar to the above (see Section 4.5 for more details). The overall fit, however, has a reduced χ^2 value of 1.4 compared to 0.8 for the isothermal case. The Polaris flare studied in Miville-Deschênes et al. (2010) has a mean intensity of 40 MJy sr^{-1} at 250 μm and $T_d = 14.5 \pm 1.6$ K, $\beta = 2.3 \pm 0.6$ when averaged over the flare. The SDP field of H-ATLAS is at least a factor of 8 fainter in the mean intensity and has a higher temperature, but a lower value for β suggesting that the dust temperature and β vary substantially across the sky depending on the intensity of the dust. This complicates simple approaches to Galactic dust modelling with one or two temperatures and β values (e.g. Finkbeiner et al. 1999). We discuss this further in Section 4.5.

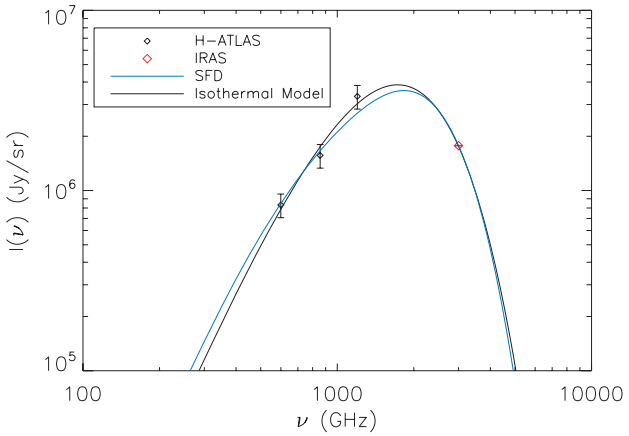

Figure 3. The Galactic dust SED averaged over the 14 deg^2 H-ATLAS SDP field and constructed by correlating SPIRE pixel intensities with 100-μm *IRAS* pixel intensity to measure the relative submm colours at each of the wavelengths (see text for details) and then scaling the *IRAS* mean flux over the field to SPIRE bands. The best-fitting dust temperature and spectral emissivity parameters are $T_d = 19.0 \pm 2.4$ K and $\beta = 1.4 \pm 0.4$, respectively (black solid line). For reference, we also show the expected SED following Schlegel et al. (1998) dust map and Finkbeiner et al. (1999) frequency scaling that involves two temperature components (see Section 4.5; blue solid line).

4.3 SEDs of bright cirrus regions

Instead of the average (T_d, β) values over the whole field, we also study the SEDs in five bright cirrus regions that are identified 1–5 in Fig. 1. The previous SED measurement made use of the SPIRE maps that were corrected for submm colour, G, and S_0 values obtained by correlating with the *IRAS* 100-μm map over the whole field and at the pixel scale of *IRAS*. To study the SED of bright regions, we now consider a differential measurement so that we can determine the SED independent of the *IRAS* 100-μm intensity in the SDP field. To account for both the extragalactic background and the zero-point, we remove from the three SPIRE maps the mean intensity from the two low-cirrus regions identified with rectangles in Fig. 1. These two regions have intensities that are at the low end of SPIRE intensities plotted in Fig. 2 and, with the previous zero-level included, these intensities are 1.6, 1.2 and 0.9 (± 0.1) MJy sr^{-1} at 250, 350 and 500 μm, respectively. We do the same for the *IRAS* map and remove the mean intensity of 1.9 (± 0.1) MJy sr^{-1} at 100 μm determined for the same two regions. This is necessary to avoid introducing an unnecessary difference in the relative calibration between SPIRE and *IRAS*. We account for the uncertainty in this mean removal in our overall error budget.

Table 1. Dust intensity and SED properties of selected high-intensity features from the SDP map.

Region #	1	2	3	4	5
RA (°)	137.44	136.18	135.69	134.79	136.35
Dec. (°)	2.39	1.90	1.63	1.47	−0.31
Area (deg^2)	0.33	0.063	0.29	0.18	0.14
Flux 100 μm (MJy sr^{-1})	1.2 ± 0.1	1.5 ± 0.1	1.6 ± 0.1	1.2 ± 0.1	0.9 ± 0.1
Flux 250 μm (MJy sr^{-1})	2.4 ± 0.4	3.5 ± 0.5	3.3 ± 0.5	2.7 ± 0.4	1.8 ± 0.3
Flux 350 μm (MJy sr^{-1})	1.1 ± 0.2	1.8 ± 0.3	1.6 ± 0.3	1.3 ± 0.2	0.7 ± 0.1
Flux 500 μm (MJy sr^{-1})	0.5 ± 0.1	0.9 ± 0.1	0.8 ± 0.1	0.7 ± 0.1	0.4 ± 0.1
ln A	-9.1 ± 0.9	-9.2 ± 0.8	-9.0 ± 0.9	-9.5 ± 0.9	-9.3 ± 1.1
β	1.8 ± 0.5	1.4 ± 0.4	1.6 ± 0.5	1.4 ± 0.5	1.9 ± 0.6
T_d	17.6 ± 2.3	18.3 ± 2.2	18.1 ± 2.5	18.3 ± 2.5	17.4 ± 2.9
χ^2	0.8	0.5	0.6	1.1	2.7

This procedure allows us to treat the *IRAS* intensity independent of SPIRE, but the results we show here do not strongly depend on this additional step. When we simply used the *IRAS* S_0 corrected maps, with SPIRE zero-level fixed to *IRAS*, we still recover SEDs that have β and T_d values consistent within uncertainties. The new maps, however, lead to differences in the amplitude due to the overall shift in the intensity scale. Another way to think about this is that β and T_d estimates extracted from the isothermal SED depend on the intensity ratios and not the absolute intensity. The noise is computed by averaging the noise intensity of pixels in the same region as defined for the intensity measurements. We add quadratically the flux error, the error in the intensity removed from the two low-cirrus regions and an overall calibration error taken to be 15 per cent of the intensity (Swinyard et al. 2010). The intensity values of the five selected regions are summarized in Table 1. We find the dust temperature of these bright cirrus regions are around 18 ± 3K with β around 1.5 ± 0.5, and consistent with results found for large-scale cirrus observations at high Galactic latitudes with a dust temperature of 17.5 K (Boulanger et al. 1996).

4.4 Relation between β and T_d

Beyond the bright regions, we also establish the dust temperature and modified spectral emissivity parameter over the whole SDP area. This allows us to produce maps of T_d and β over the SDP field. To this aim, we repixelize all maps to 6×6 arcmin^2 pixels resulting in a grid of 55×55 pixels for the H-ATLAS SDP field; with smaller pixel sizes we get noisier estimates of T_d and β in regions of low cirrus intensity, while with larger pixels we do not sample the map adequately. The reprojection is done such that the flux is preserved when going from smaller pixels to 6-arcmin pixels. This particular choice of pixel size was made so that the total number of grid points used for (A, T_d, β) model fits can be completed in a reasonable time (a few days in this case) given the computational costs associated with generating separate MCMC chains. Here again we consider a differential measurement and remove the mean intensity estimated in low-cirrus parts (before the maps were repixelized) and in those regions we set $A = 0$ with the assumption of no cirrus.

With this analysis, we construct the two maps that we show in Fig. 4, where we subselect 6-arcmin pixels where the SED fits gave relative errors less than 30 per cent for both parameters β and T_d. These values are also plotted in Fig. 5. They mostly span the high-intensity region of the SDP map. For reference, in Fig. 6 (left-hand panels) we show the maps of T_d and β without this selection imposed. At first glance, β and T_d appear to be negatively correlated. Part of this correlation results from the functional form

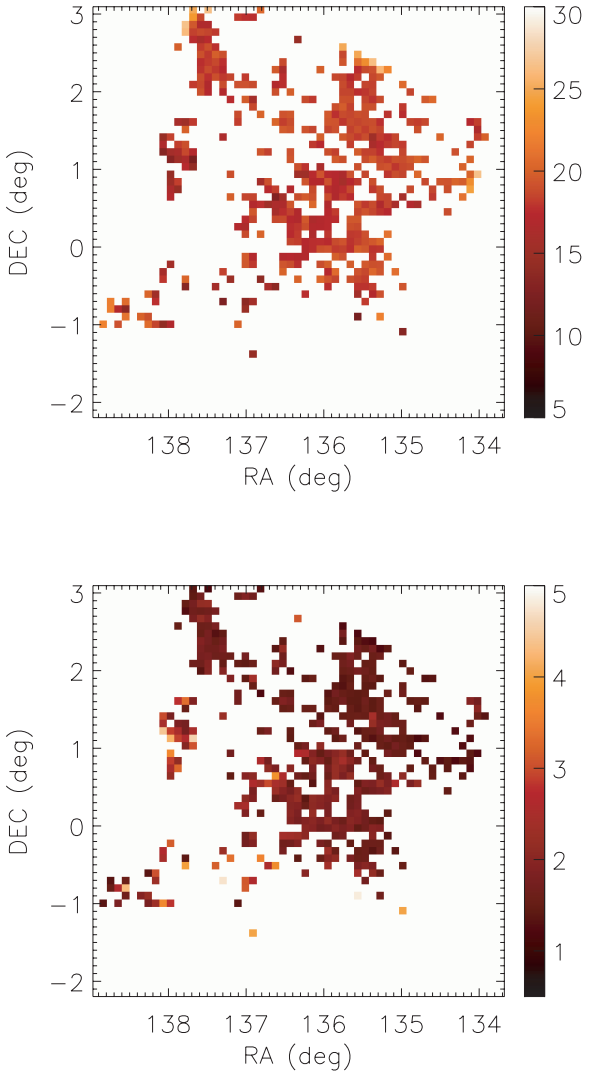

Figure 4. The dust temperature (top) and spectral emissivity parameter β (bottom) based on our SED fits to pixel intensities that survive the requirement that the two parameters be measured with relative uncertainty (1σ) better than 30 per cent.

of the equation (3) that we used to fit the intensity data, especially in the presence of noise (Shetty et al. 2009a).

In order to discriminate any physical effect from the analytical correlation, we test two possible models that describe the β versus

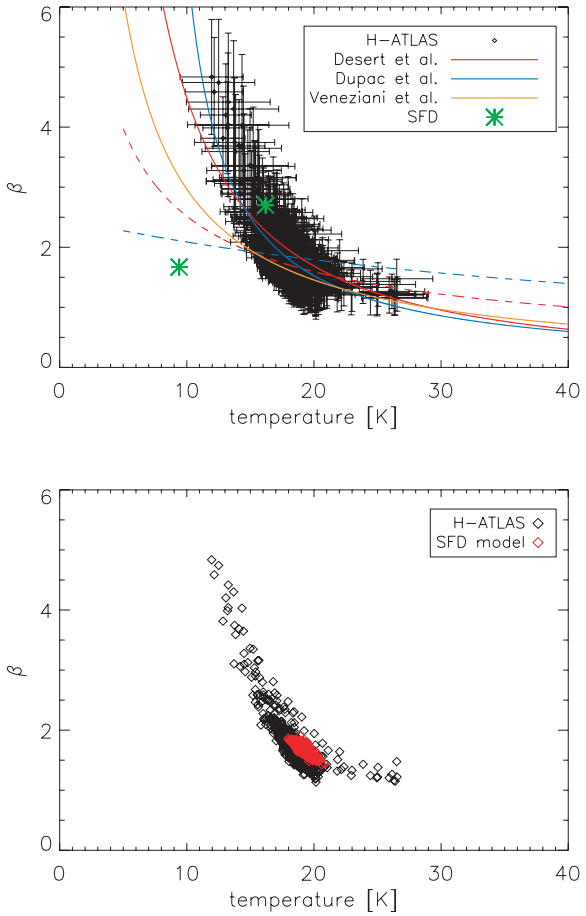

Figure 5. Top panel: best-fitting values of the spectral emissivity parameter, β, and dust temperature, $T_{\rm d}$, over the whole SDP field with all maps repixelized at 6-arcmin pixels. The error bars show the 1σ uncertainties of these two parameters in each of the pixels. The dashed lines show the best-fitting models for $T_{\rm d}$ versus β based on the two analytical descriptions outlined in Section 4.4 with parameter values from Dupac et al. (2003) and Désert et al. (2009). The solid lines show the same model descriptions but with the parameters obtained in this work. We also compare the best-fitting line of Veneziani et al. (2010) from observations of high-density clouds in the BOOMERanG-2003 CMB field. Compared to previous measurements that studied high-density dust regions, we find a stronger anti-correlation for diffuse emission. The noise-weighted mean values of $T_{\rm d}$ and β are 20.1 ± 1.6 K and 1.5 ± 0.3, respectively. These are somewhat better than the previous estimates over the whole area as we exclude pixels which have relative errors for $T_{\rm d}$ and β that are greater than 30 per cent. The two points show $T_{\rm d}$ and β of Finkbeiner et al. (1999) model-8 used to scale the dust map of Schlegel et al. (1998). Bottom panel: comparison between best-fitting $T_{\rm d}$ and β distribution with same parameters in the same pixels from the Schlegel et al. (1998) dust model (see text for details).

$T_{\rm d}$ dependence, either with

$$\beta(T_{\rm d}) = N T_{\rm d}^{\alpha}, \tag{4}$$

following Désert et al. (2009), or

$$\beta(T_{\rm d}) = \frac{1}{C + x T_{\rm d}}, \tag{5}$$

from Dupac et al. (2003).

Instead of simply using the best-fitting $T_{\rm d}$ and β values and their variances when doing a fit to the two forms of $\beta(T_{\rm d})$ given above, we need a numerical method that also takes into account the full covariance between the two parameters at each of the pixels. To achieve this, we fit for the two parameters describing each of the relations between β and $T_{\rm d}$ by making use of the full probability distributions captured by the MCMC chains. The procedure we use is the same as that of Veneziani et al. (2010).

A basic summary of the approach is that we fit, for example N and α, by drawing random pairs of β and $T_{\rm d}$ by sampling their likelihood functions from the MCMC chains we had first generated by fitting the isothermal SED models to individual pixel intensities; here again, we restrict the analysis to chains where β and $T_{\rm d}$ are determined with relative errors better than 30 per cent for both parameters.

By using the full MCMC chains to sample β and $T_{\rm d}$ directly, we keep information related to the full covariance and this takes into account the fact that β and $T_{\rm d}$ are anti-correlated in each of the pixels that we use for this analysis. For each of the two forms of $\beta(T_{\rm d})$, we sample the chains by drawing 20 000 random pairs of β and $T_{\rm d}$; we established a sampling of 20 000 is adequate by a series of simulations using anti-correlated data points in the $\beta - T_{\rm d}$ diagram with errors consistent with Fig. 5 and assuming random correlation coefficients of -0.3 to -0.8. Through this fitting procedure, we extract the distribution functions of the four parameters N, α, C and x, and these in return allow us to quote their best-fitting values and errors.

We find $[N, \alpha]$ of $[N = 116 \pm 38, \alpha = -1.4 \pm 0.1]$ and $[C, x]$ of $[C = -0.36 \pm 0.02, x = (5.1 \pm 0.1) \times 10^{-2}]$. We show these two best-fitting lines in Fig. 5. The two models have χ^2 per degree-of-freedom values of 0.8 and 0.5, respectively, suggesting that the model of Dupac et al. (2003) is slightly preferred over the other. With reduced χ^2 values less than one, it is likely that we are also overestimating our overall error budget, especially with the 15 per cent flux calibration uncertainty. In Swinyard et al. (2010), the calibration error for SPIRE data is stated with an additional safety margin and the likely error is between 5 and 10 per cent. For comparison, Désert et al. (2009) found $[N = 11.5 \pm 3.8, \alpha = -0.66 \pm 0.05]$, while Dupac et al. (2003) found $C = 0.40 \pm 0.02$ and $x = (7.9 \pm 0.5) \times 10^{-3}$. These two lines, as well as the best-fitting line of Veneziani et al. (2010), are shown in Fig. 5 for comparison. The Veneziani et al. (2010) measurements involve seven high-density clouds in the BOOMERanG-2003 CMB field and their measurements are consistent with prior works, except for one cloud with a low dust temperature of (6.5 ± 2.6) K and β of 5.1 ± 1.8.

While we find β values as high as 4–5, most of the values are between 1 and 3. We show three example SEDs in Fig. 7 spanning low, mid and high values of both $T_{\rm d}$ and β. Even if we constrain the study of $\beta(T_{\rm d})$ relation to the range of $1 < \beta < 3$, we still find non-zero values for the four parameters N, α, C and x consistent with above values, suggesting that there is an intrinsic anti-correlation and not driven by the few high β points.

Fig. 5 demonstrates two interesting scientific results: (i) we find an underlying relation between $T_{\rm d}$ and β that cannot be due to an anti-correlation induced by noise when fitting the SED form to pixel intensities and (ii) we find a higher value of β at low dust temperatures compared to the values suggested by previous relations in the literature. Our result shows that the anti-correlation also exists for low-intensity Galactic cirrus and is not limited to high-density clumps and molecular clouds that were previously studied. It is likely that the $T_{\rm d}$ versus β relation captures different physical and chemical properties of the dust grains, including the size distribution and the interstellar radiation field that heat the dust. There is also a possibility that this anti-correlation results from line-of-sight projection of different dust temperature components (Shetty et al. 2009b). With the field at a Galactic latitude of 30°, such overlap is

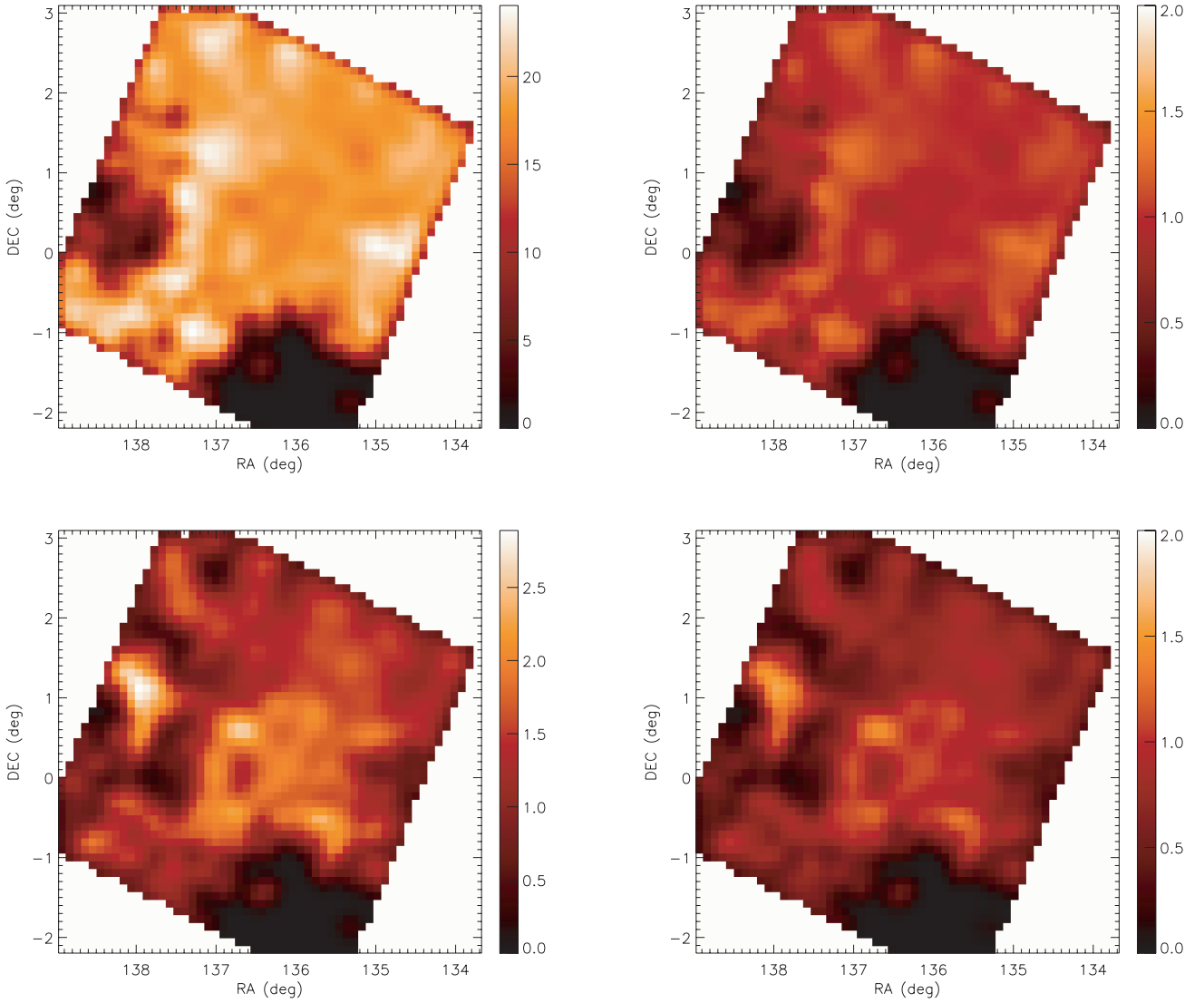

Figure 6. Top-left panel: map of the dust temperature; best-fitting values are shown. Units are in kelvin. Pixels with $T_{\rm d} < 5$ K are dominated by noise and should not be considered as an accurate measurement. Fig. 4 shows the subselection where $T_{\rm d}$ and β are determined with a relative accuracy better than 30 per cent. Top-right panel – ratio map between data temperature map and a map of the dust temperature by re-analysing the Schlegel et al. (1998; SFD) dust map for the same region scaled by model 8 of the Finkbeiner et al. (1999) two temperature description and refitted with our isothermal SED following the same procedure as data. Bottom-left panel: map of spectral emissivity parameters β; best-fitting values are shown. Bottom-right panel: map of the ratio between data spectral emissivity map and the spectral emissivity map derived from the SFD model dust map similar to dust temperature.

likely to be small, but perhaps not completely negligible. Unfortunately we do not have a way to constrain the line-of-sight projection due to the lack of distance information. Also, studies on the β and $T_{\rm d}$ relation are so far limited to handful of fields and more work is clearly desirable. We note that laboratory measurements have suggested the possibility of such an anti-correlation for certain types of dust grains (e.g. Agladze et al. 1996; Mennella et al. 1998; Boudet et al. 2005). This has been explained as due to quantum physics effects on the amorphous grains, such as due to two-phonon processing and tunnelling effects between ground states of multilevel systems. Whether the relation we have observed is due to averaging different values of temperature along the line of sight or due to an intrinsic property of dust is something that will remain uncertain.

Related to the observation (ii) outlined above, the measurements we report here are primarily dominated by the diffuse cirrus emission over the whole SDP area. The Dupac et al. (2003) relation was for a large sample of molecular clouds in the Galaxy while the Désert et al. (2009) measurements involve a sample of cold clumps detected as point sources in the Archeops CMB experiment. The dust size distribution is expected to be different in denser regions compared to that in diffuse cirrus as the small grains are expected to coagulate into large aggregates. The diffuse cirrus is likely dominated by small grains and this difference could be captured in terms of different values of β for a given $T_{\rm d}$. The expectation is that denser regions would show smaller values of β (e.g. Ossenkopf & Henning 1994), consistent with Fig. 5. Once *Herschel* imaging data have been obtained for more of the H-ATLAS areas, it will be interesting to study the $T_{\rm d}$ and β relation for a variety of source structures, from dense cores and clumps in our Galaxy to extragalactic sources to diffuse Galactic cirrus emission in order to establish how the relation changes with the environment. Both the *Herschel* Infrared Galactic Plane Survey (Hi-GAL) survey with *Herschel* (Molinari

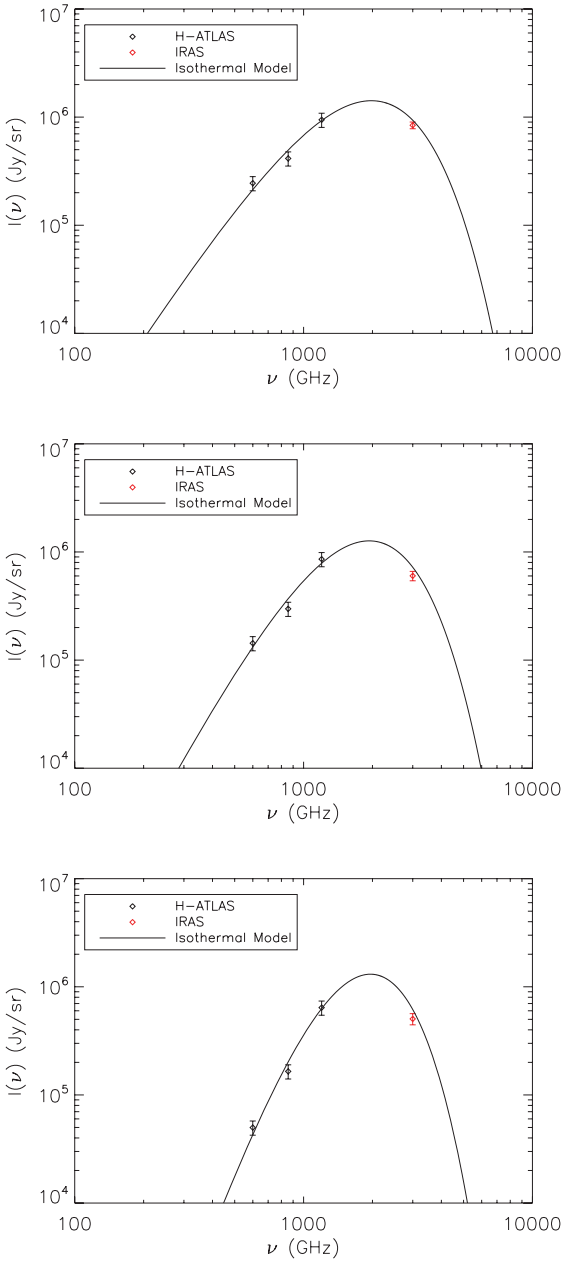

Figure 7. Example SEDs showing SPIRE and *IRAS* 6-arcmin pixel intensities and the best-fitting isothermal model with $T_{\rm d} = 20.1$ and $\beta = 1.3$ (top), $T_{\rm d} = 18.2$ and $\beta = 2.1$ (middle), and $T_{\rm d} = 13.1$, $\beta = 4.0$ (bottom).

et al. 2010) and *Planck* can make important contributions to this topic in the future.

4.5 Comparison to a dust model

We compare our β and $T_{\rm d}$ maps with analogous maps obtained through model 8 of Finkbeiner et al. (1999) following the dust model of Schlegel et al. (1998; SFD hereafter). The SFD dust map is produced by combining 100-μm *IRAS* and 240-μm *COBE*/DIRBE data and is an all-sky map of submm and microwave emission of the diffuse interstellar dust. The model 8 of Finkbeiner et al. (1999) involves two dust temperature components at 9.2 and 16.2 K with $\beta = 1.67$ and 2.70, respectively (see the two points in Fig. 5). The SFD dust map with a frequency scaling such as model 8 is heavily utilized by the CMB experimental community both in planning and quantifying the Galactic dust contamination in CMB anisotropy measurements. At tens of degree angular scales and at frequencies above 90 GHz, Galactic dust is expected to be the dominant foreground contamination, especially for polarization measurements of the CMB (e.g. Dunkley et al. 2009).

In order to compare the measurements in the SDP field to predictions from the SFD map combined with Finkbeiner et al. (1999) frequency scaling for dust emission, we make a new set of maps at 100, 250, 350 and 500 μm using the SFD dust map and overlapping with the H-ATLAS SDP field (Fig. 8 shows a comparison of maps at 250 μm). We analysed these four simulated maps by applying the same procedure as we used for extracting spectral emissivity parameter and dust temperature with SPIRE and *IRAS* real maps. We also include the SPIRE noise making use of the SPIRE noise maps of the field generated from the data. We obtain two maps from the SFD dust map, one connected to the spectral emissivity β and one related to the dust temperature $T_{\rm d}$.

We show the ratio map between data and SFD model results for both spectral emissivity and dust temperature in Fig. 6 (right-hand panels), while the left-hand panels show our measurements directly on SPIRE data. The two component dust model of Finkbeiner et al. (1999) only captures a limited range of dust temperature and β. The model involves a low-dust temperature component at 9.2 K with $\beta = 1.67$; SPIRE maps spanning out to 500 μm are not strongly sensitive to such a cold dust component though such a cold component primarily impacts the mm-wave data. We find that the mid-values are safely produced by the SFD model, but is not a reliable description for regions that have either low or high temperatures. Such regions have either low or high β values due to the anti-correlation between the two parameters. Wide-field imaging with *Herschel*, such as the existing H-ATLAS and the proposed *Herschel*-SPIRE Legacy Survey (Cooray et al. 2010) and *Planck*, will provide necessary information to improve the Galactic dust map and the associated frequency scaling model as a function of the sky position. While in this work, we only considered the 14 deg^2 SDP field, the South Galactic Pole (SGP) and North Galactic Pole (NGP) portions of H-ATLAS each cover about 200 deg^2, will significantly improve the *IRAS*-based dust model of our Galaxy, especially at Galactic latitudes probed by CMB experiments. In a future paper, we will return to a further analysis on the improvements necessary for the dust model with data in those wide fields.

5 CIRRUS POWER SPECTRUM

Given that SPIRE is capable of mapping the diffuse emission at large angular scales, we also study the angular power spectrum related to cirrus emission for each of the wavelength bands. For this measurement, we keep the maps at the original pixel scale (Section 2) and compute the power spectrum of the intensity in maps masked for detected sources. With 1–5 per cent of the pixels masked, we found the mode coupling introduced by the source mask to be negligible.

We show our measurements in Fig. 9. At $k > 0.1$ arcmin^{-1}, the effects of the beam transfer function become important but we do not make a correction for the beam here as we are mostly interested in the power spectrum at degree angular scales, where the transfer function related to the SPIRE beam is effectively one (Martin et al. 2010; Miville-Deschênes et al. 2010; Amblard et al. 2011). In addition to the beam, there is also the map-making transfer function associated with any filtering employed during the map-making

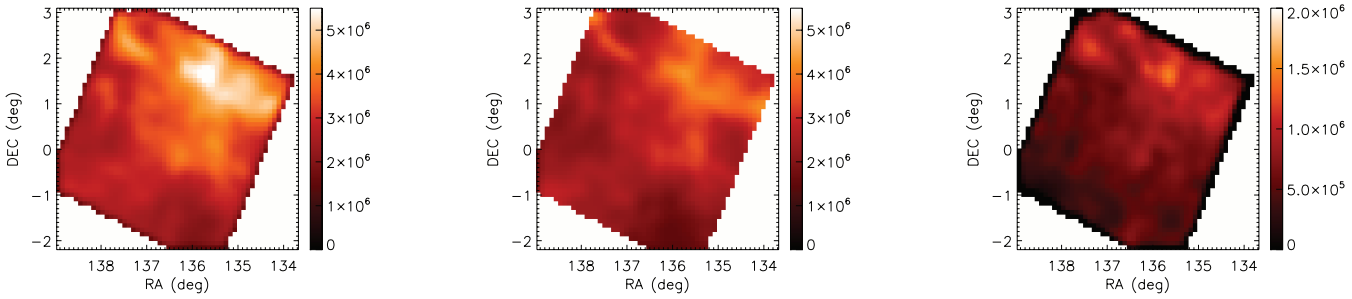

Figure 8. Left-hand panel: SPIRE 250-μm map of H-ATLAS SDP field at the 6-arcmin pixel resolution used for studying β and $T_{\rm d}$ over the whole map (Section 4.4). Middle panel: a map of the same field extracted from the Schlegel et al. (1998) dust map with Finkbeiner et al. (1999) model-8 frequency scaling to obtain 250-μm intensities at the same 6-arcmin pixel resolution. Right-hand panel: a map showing the difference between the observed data and the extrapolation from the Schlegel et al. (1998) dust map with Finkbeiner et al. (1999) model-8 frequency scaling. All three maps are in units of Jy sr^{-1}. To highlight the difference map, the third map has a shorter colour stretch.

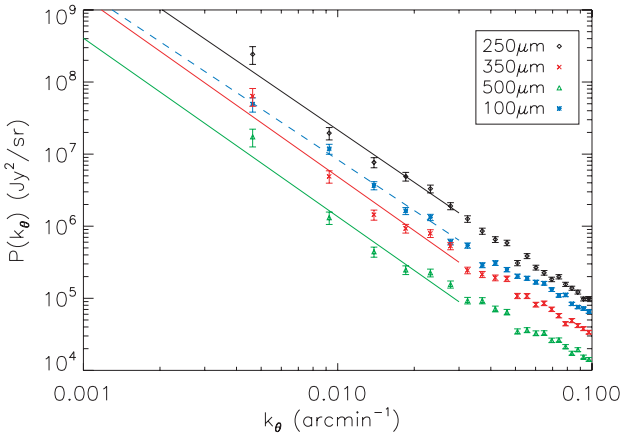

Figure 9. Angular power spectrum of the H-ATLAS field associated with Galactic cirrus. The power-law model fits are considered down to k of 0.03 arcmin^{-1} to avoid the cirrus measurements with extragalactic background fluctuations that are expected to peak at $k \sim 0.1$ arcmin^{-1}.

process (Pascale et al. 2011). At the angular scales of interest, this transfer function is also consistent with one.

We assume a power spectrum of the form $P(k) = P_0(k/k_0)^{\gamma}$ to describe the measurements and take $k_0 = 0.01$ arcmin^{-1} to be consistent with previous studies. Using data out to $k < 0.03$ arcmin^{-1}, to avoid contamination with fluctuations associated with the extragalactic background, we find $\gamma = -2.4 \pm 0.1$ at 100 μm with *IRAS* and -2.6 ± 0.2 at each of the SPIRE bands at 250, 350 and 500 μm. The measured values of the fluctuation amplitudes are $P_0 = (8.3 \pm 0.7) \times 10^6$, $(2.2 \pm 0.2) \times 10^7$, $(4.8 \pm 0.5) \times 10^6$ and $(1.3 \pm 0.1) \times 10^6$ at 100, 250, 350 and 500 μm, respectively (in units of Jy^2 sr^{-1}). The normalization at 100 arcmin^{-1} angular scale we find for *IRAS* 100 μm map is fully consistent with the relation between $P(k = 0.01)$ and the mean 100-μm intensity in Miville-Deschênes et al. (2002; see their fig. 4), given the *IRAS* mean intensity of 1.77 MJy sr^{-1} in the SDP field. The power-law slope γ we find is somewhat lower than measurements for the slope in the literature [e.g. Miville-Deschênes et al. (2010) with a slope if -2.7 ± 0.1 and Martin et al. (2010) with slopes of -2.74 ± 0.03 and -2.81 ± 0.03 in two separate fields], but consistent with the analysis in Roy et al. 2010 (with a slope of -2.6 ± 0.07 at 250 μm). All these measurements are consistent with each other given the overall uncertainties. It could also be that our slope is lowered by tens of per cent level due to fluctuations associated with the extragalactic background. If we constrain to $k < 0.01$ arcmin^{-1}, keeping only two data points, we do find a higher slope closer to -2.8 to -2.9 but with larger uncertainty ($\pm$ 0.4).

The $\sqrt{k^2 P(k)/2\pi}$ captures the rms fluctuations over the whole SDP area arising from Galactic cirrus and the extragalactic background at a given value of the wavenumber. At large angular scales, the fluctuations generated by the extragalactic sources (mainly the sources contributing the background confusion noise) are subdominant with values of order 10^4–10^5 Jy^2 sr^{-1} in $P(k)$ when $k <$ 0.01 arcmin^{-1} (say at 250 μm; Amblard et al. 2011). For comparison, in Fig. 9 we find Galactic cirrus fluctuations at the level of 10^7–10^9 Jy^2 sr^{-1}. Thus, at $k = 0.01$ arcmin^{-1} we can safely assume that all of the fluctuations we have measured arise from Galactic cirrus. Taking the $\sqrt{(P_0)}$ values, we can make an independent estimate of the dust temperature and β similar to the analysis of Martin et al. (2010). We find $T_{\rm d} = 20.1 \pm 0.9$ K and $\beta = 1.3 \pm 0.2$, consistent with the same two quantities we obtained in Section 4.2 by cross-correlating SPIRE maps with *IRAS*.

6 SUMMARY AND CONCLUSIONS

In this paper, we have studied the Galactic dust SED and the angular power spectrum of dust fluctuations in the 14 deg^2 SDP field of H-ATLAS. By correlating the SPIRE 250, 350 and 500 μm and *IRAS* 100-μm maps to extract the submm colour terms of SPIRE maps relative to the *IRAS* 100-μm map of the SDP field, we find the average dust temperature over the whole field to be 19.0 $\pm$ 2.4 K with the spectral emissivity parameter taking a value of 1.4 $\pm$ 0.4. We find all of the bright cirrus regions to have dust temperatures $T_{\rm d}$ over a narrow range of 17.4–18.3 K ($\pm$ 2.5 K), with a spectral emissivity parameter β ranging from 1.4 to 1.9 ($\pm$0.5). Similar to previous studies, we find an anti-correlation between $T_{\rm d}$ and β; when described by a power law with $\beta = AT_{\rm d}^{\alpha}$, we find $A = 116 \pm 38$ and $\alpha = -1.4 \pm 0.1$, while a relation of the form $\beta = (C + xT_{\rm d})^{-1}$ is also consistent with data with $C = -0.36 \pm 0.02$ and $x = (5.1 \pm 0.1) \times 10^{-2}$. The observed inverse relation between $T_{\rm d}$ and β is stronger than the previous suggestions in the literature, and we have suggested the possibility that this stronger anti-correlation may be due to the fact that we study primarily diffuse cirrus while previous studies involved high-density environments such as molecular clouds and cold clumps. We also make an independent estimate of the dust temperature and the spectral emissivity parameter, when averaged over the whole field, through the frequency scaling of the rms amplitude of dust fluctuation power spectrum. At 100-arcmin angular scales, we obtain $T_{\rm d} = 20.1 \pm 0.9$ K and $\beta = 1.3$ $\pm$ 0.2, consistent with previous estimates. The cirrus fluctuations

power spectrum is consistent with a power law at 100, 250, 350 and 500 μm with a power-law spectral index of -2.6 ± 0.2 from 1 to 200-arcmin angular scales.

After we completed this paper, we became aware of a similar study involving the β and $T_{\rm d}$ in the first two fields covered by the Hi-GAL survey (Paradis et al. 2010). These authors also find an anti-correlation between the two parameters, but the mean relation is distinctively different between the two fields at Galactic longitudes of 30° and 50°, with both on the Galactic plane. When compared to the H-ATLAS SDP field, these two fields have mean intensities that are a factor of 200 larger at the level of 1000 MJy sr^{-1}. Interestingly the $\beta(T_{\rm d})$ relation they find for the field at $l = 30^\circ$ is consistent with the relation we report here when extrapolating their relation that was determined over the range of $1.5 < \beta < 2.5$ and $18 < T_{\rm d}/{\rm K} < 25$ to lower 14 K dust temperatures we find in some of the pixels in our field with $\beta \sim 4$. It could very well be that the dust properties are far more complex than the simple isothermal models we have considered and a variety of effects may be contributing to the observed anti-correlation. Further studies making use of wide area maps are clearly warranted.

ACKNOWLEDGMENTS

The *Herschel*-ATLAS is a project with *Herschel*, which is an ESA space observatory with science instruments provided by European-led Principal Investigator consortia and with important participation from NASA. The H-ATLAS website is http://www.h-atlas.org/. AA, AB, AC and PS acknowledge support from NASA funds for US participants in *Herschel* through JPL.

REFERENCES

Agladze N. I., Sievers A. J., Jones S. A., Burlitch J. M., Beckwith S. V. W., 1996, ApJ, 462, 1026
Amblard A. et al., 2011, Nat, in press
Bernard J. P. et al., 1999, A&A, 347, 640
Bot C., Helou G., Latter W. B., Puget J., Schneider S., Terzian Y., 2009, ApJ, 695, 469
Boudet N., Mutschke H., Nayral C., Jäger C., Bernard J. P., Henning T., Meny C., 2005, ApJ, 633, 272
Boulanger F. et al., 1996, A&A, 312, 256
Clements D. et al., 2010, A&A, 518, L8
Cooray A. et al., 2010, preprint (arXiv:1007.3519)
Désert F.-X., Boulanger F., Puget J.-L., 1990, A&A, 215, 236
Désert F.-X. et al., 2009, A&A, 411, 481
Dunkley J. et al., 2009, in Dodelson S. et al., eds, AIP Conf. Ser. Vol. 1141, CMB Polarization Workshop: Theory and Foregrounds. Am. Inst. Phys., New York, p. 222
Dupac X. et al., 2003, A&A, 404, L11
Driver S. P. et al., 2009, Astron. Geophys., 5.12, 5.19
Eales S. et al., 2010, PASP, 499, 515
Finkbeiner D. P., Davis M., Schlegel D. J., 1999, ApJ, 524, 867
Fixsen D. J., Dwek E., Mather J. C., Bennett C. L., Shafer R. A., 1998, ApJ, 508, 106
Gelman A., Rubin D. B., 1992, Statistical Sci. 7, 457
Griffin M. J. et al., 2010, A&A, 518, L3
Ibar E. et al., 2010, MNRAS, submitted
Jeong W.-S., Mok Lee H., Pak S., Nakagawa T., Minn Kwon S., Pearson C. P., White G. J., 2005, MNRAS, 357, 535
Lagache G., Haffner L. M., Reynolds R. J., Tufte S., 2000, A&A, 354, 247
Leach S. M. et al., 2008, A&A, 597, 615
Levenson L. et al., 2010, MNRAS, submitted
Lewis A., Bridle S., 2002, Phys. Rev. D., 66, 103511
Low F. J., Neugebauer G., Gautier T. N., III, Gillett F., 1984, BAAS, 16, 968
Martin P. G. et al., 2010, A&A, 518, L105
Mennella V., Brucato J. R., Colangeli L., Palumbo P., Rotundi A., Bussoletti E., 1998, ApJ, 496, 1058
Meny C., Gromov V., Boudet N., Bernard J.-P., Paradis D., Nayral C., 2007, A&A, 468, 471
Miville-Deschênes M.-A., Lagache G., 2005, ApJS, 157, 302
Miville-Deschênes M.-A., Lagache G., Puget J.-L., 2002, A&A, 749, 756
Miville-Deschênes M.-A. et al., 2010, A&A, 518, L104
Molinari S. et al., 2010, A&A, 518, L100
Oliver S. et al., 2010, A&A, 518, L21
Olmi L. et al., 2010, preprint (arXiv:1005.1273)
Ossenkopf V., Henning Th., 1994, A&A, 291, 943
Ott S. et al., 2006, in Gabriel C., Arviset C., Ponz D., Solano E., eds, ASP Conf. Ser. Vol. 351, Astronomical Data Analysis Software and Systems XV. Astron. Soc. Pac., San Francisco, p. 516
Paradis D., Bernard J.-P., Mény C., 2009, A&A, 506, 745
Paradis D. et al., 2010, A&A, 520, L8
Pascale E. et al., 2011, MNRAS, submitted (arXiv:1010.5782)
Pilbratt G. L. et al., 2010, A&A, 518, L1
Ricciardi S. et al., 2010, MNRAS, 1644, 1658
Rigby E. et al., 2011, MNRAS, submitted (arXiv:1010.5787)
Roy A. et al., 2010, ApJ, 708, 1611
Sadavoy S. I., Di Francesco J., Johnstone D., 2010, ApJ, 32, L37
Schlegel D. J., Finkbeiner D. P., Davis M., 1998, ApJ, 500, 525
Shetty R., Kauffmann J., Schnee S., Goodman A. A., 2009a, ApJ, 696, 676
Shetty R., Kauffmann J., Schnee S., Goodman A. A., Ercolano B., 2009b, ApJ, 696, 2234
Swinyard B. et al., 2010, A&A, 518, L4
Veneziani M. et al., 2010, ApJ, 959, 969
Wang L., Rowan-Robinson M., 2009, MNRAS, 398, 109
Ward-Thompson D. et al., 2010, A&A, 518, L92

This paper has been typeset from a TEX/LATEX file prepared by the author.